Experimental Validation of String Stability for Connected Vehicles Subject to Information Delay

Wubing B. Qin and Gábor Orosz

***Abstract*— In this paper, we investigate the performance of communication-based controller design in connected vehicle networks. A testbed consisting of a group of ground robots that can mimic the dynamics of personal vehicles is built. We show that when incorporating time delays in the modeling equations, which arise due to digital implementation and intermittent vehicle-to-vehicle (V2V) communication, the experimental results have a very good correspondence with the theoretical ones. Moreover, we demonstrate that by designing a controller for each individual vehicle in the chain plant stability and string stability can be guaranteed despite the time delays in the control loop. Then, a series of experiments is conducted for a mixture of string stable and string unstable vehicles and the effects of penetration rate of string stable vehicles in maintaining smooth traffic are evaluated. The results lay a foundation for connected vehicle system design with flexible connectivity topologies.**

***Index Terms*— Connected automated vehicle (CAV), ground robots, penetration rate, string stability, vehicle-to-everything (V2X) communication.**

I. Introduction

THE increase in the number of road vehicles over the past few decades has been causing more frequent traffic congestion [1] and accidents [2]. To overcome the perception limitations and large reaction time of human drivers, vehicle automation may be used to enhance safety and driving comfort [3]. Some of these technologies, when designed appropriately, may also be used to improve traffic efficiency. For example, feedback information of onboard sensors may be utilized to maintain a safe distance from the vehicle ahead that may have a positive impact on traffic flow when its penetration rate of equipped vehicles is high enough [4]–[9]. This technology is referred to as adaptive cruise control (ACC) and already available on high-end personal vehicles. However, ACC requires the preceding vehicle to be within the line of sight, which may hinder its applicability on curly roads and bad weather conditions. Moreover, responding to the motion of multiple vehicles ahead (some of whom are beyond the line of sight) may significantly improve the performance of vehicles [10].

Wireless vehicle-to-everything (V2X) connectivity [11]–[13] allows vehicles to obtain motion information from neighboring vehicles within and beyond the line of sight. The related communication technologies have been standardized by different international organizations [14]–[18] in the U.S. [19], Europe [20], Japan [21], and China [22]. These standards allow vehicles to "speak the same language." When a human-driven vehicle is equipped with V2X devices, we obtain a so-called connected human-driven vehicle (CHV). The penetration rate of CHVs is expected to increase rapidly in the near future since major automotive manufacturers have started to deploy V2X technology on production vehicles. When a vehicle can control its motion using onboard controllers, we obtain an automated vehicle (AV). Moreover, when V2X information is included in the motion controllers of an AV, we obtain a so-called connected AV (CAV). To fully exploit the advantages of V2X communication, a CAV may gather information from multiple vehicles within communication range [23]–[25] (whom may be beyond the line of sight) and this way achieve a more complete perception of the surrounding traffic.

CAV can utilize different control technologies in motion controllers, such as cooperative adaptive cruise control (CACC) and connected cruise control (CCC). CACC [26]–[34] refers to cooperative algorithms where a group of CAVs travel together. In CACC, high level of automation allows vehicles to cooperate. Fruitful simulations [35]–[40] and experiments [41]–[48] have been conducted to show the potential benefits of such connectivity structure. However, until the penetration rate of CAVs reaches 100%, vehicles at different levels of automation [49] need to be dealt with which includes human-driven vehicles and AVs without V2X devices. CCC refers to non-cooperative algorithms where CAVs utilize all available V2X information from vehicles ahead. We emphasize that CCC does not require other vehicles to be CHVs or AVs, but can still achieve system-level benefits even when only a few other vehicles support V2X connectivity. To better understand CCC, many aspects have been studied theoretically, such as communication delays, connectivity topologies, nonlinearities, optimality, and predictor design [50]–[59]. On the other hand, no experimental validation has been carried out to prove the feasibility of this concept.

Manuscript received August 28, 2018; revised January 14, 2019; accepted February 5, 2019. Date of publication April 11, 2019; date of current version June 11, 2020. Manuscript received in final form February 16, 2019. This work was supported by the National Science Foundation under Grant 1300319. Recommended by Associate Editor N. van de Wouw. *(Corresponding author: Wubing B. Qin.)*

The authors are with the Department of Mechanical Engineering, University of Michigan, Ann Arbor, MI 48109 USA (e-mail: wubing@umich.edu; orosz@umich.edu).

Color versions of one or more of the figures in this article are available online at http://ieeexplore.ieee.org.

Digital Object Identifier 10.1109/TCST.2019.2900609

In this paper, we aim at bridging the gap between theoretical analysis and experimental validation, utilizing a scaled connected vehicle testbed consisting of ground robots. The robots are designed such that they could capture the longitudinal and lateral dynamics of full-size vehicles when scaled up. That is, the controller design of the robots provides us with insights about the controller design of real vehicles. For verification purposes, we start with the simplest connectivity topology, i.e., (cascaded) predecessor-follower systems and study vehicle dynamics and traffic performance. This paper will be the foundation for the follow-up experimental research on more complex connectivity topologies in CCC systems. We incorporate the time delays arising in the control loop due to intermittent vehicle-to-vehicle (V2V) communication and digital implementation [60] and derive theoretical conditions to ensure string stability. The experiments demonstrate that the obtained theoretical results can capture the behavior of the robots. This allows us to design string stable vehicles in the presence of time delays and also show that inappropriate design may lead to string instability.

First, using the connected vehicle testbed, we experimentally demonstrate how human drivers amplify fluctuations in traffic flow and how CAVs attenuate fluctuations to improve the overall traffic performance. We show that when all vehicles are human driven, fluctuations are gradually amplified and stop-and-go traffic jams [61], [62] are likely to happen. On the other hand, when all vehicles are string stable CAVs, fluctuations are damped down such that traffic jams are less likely to be triggered. Second, we study what percentage of CAVs is needed in order to improve overall traffic performance. We investigate the behaviors for different penetration rates and distributions of string stable CAVs and string unstable human-driven vehicles. The results unveil that relatively high penetration rate of string stable CAVs is required to achieve string stability for the overall traffic if they only respond to the motion of the direct predecessor. This result motivates us to study CAVs that respond to the motion of multiple vehicles ahead utilizing more complex connectivity topologies in the follow-up research.

The remainder of this paper is organized as follows. In Section II, we propose a longitudinal controller used in the rest of this paper and set the performance requirements. In Section III, we describe the connected vehicle testbed including the mechanical structure of the robots, the electronic control system (ECS), and the software design. In Section IV, a dynamic model is presented and the stability analysis of the closed-loop system is carried out based on the digital implementation of the controller. In Section V, experiments are conducted with two robots to validate the results on string stability analysis of vehicles subject to communication delay. In Section VI, experiments are conducted on five robots and the effects of the penetration rate on traffic performance are investigated. In Section VII, conclusions are drawn and future research directions are pointed out.

II. Performance Requirements and Controller Design

In this section, we propose a longitudinal controller based on a vehicle model in the longitudinal direction and set the corresponding performance requirements. To characterize the performance of traffic systems, plant stability [51], [63], [64], string stability [65], scalability [32], [54], and throughput [66] are typically of our concern. In this paper, we focus on the first two aspects and start with their definitions for predecessor-follower system where each vehicle responds to the motion of the vehicle immediately ahead (see Fig. 1).

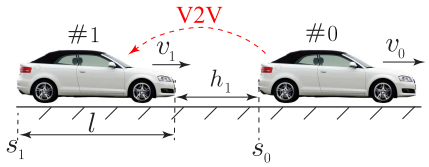

Fig. 1. Predecessor-follower system. Red dashed arrow: V2V communication.

A. Performance Requirements

A two-car predecessor-follower system is *plant stable* if the follower can asymptotically approach the same constant velocity as the predecessor. This definition may be extended to larger predecessor-follower systems as those can be constructed as concatenations of two-car predecessor-follower systems. Clearly, all vehicles must be plant stable to ensure the plant stability of the overall system. Plant instability results in divergence of velocity and may lead to collisions or crashes [54].

A two-car predecessor-follower system is *string stable* if the velocity perturbations of the predecessor are attenuated by the follower. This definition may also be extended to larger predecessor-follower systems but more careful consideration is needed. If all vehicle pairs are string stable then indeed velocity perturbations decay as they propagate along the vehicle chain and the system is string stable. Similarly, when all vehicle pairs are string unstable, a string unstable system arises which results in traffic jams [54]. However, when considering a mixture of string stable and string unstable vehicle pairs, different definitions of string stability have been proposed. In this paper, we are interested in *head-to-tail string stability* [51]. The motivation comes from scenarios where a CAV uses information from multiple vehicles ahead, so we compare the velocity fluctuations of the CAV to that of the furthest vehicle whose motion information is utilized. In this paper, we use this metric when referring to string stability of vehicle chains.

B. Dynamics and Controller Design

We start the controller design considering the two-car predecessor-follower system shown in Fig. 1 where v_0 and v_1 represent the predecessor's and the follower's velocities, respectively, whereas h_1 is the inter-vehicle distance. To model the follower's longitudinal dynamics, we consider no slip condition on the wheels and neglect the flexibility of the tires and the suspension, which results in the differential equation

$$m_{\text{eff}}\,\dot{v}_1 = -m\,g\sin\phi - \mu\,m\,g\cos\phi - b\,v_1 - \nu\,(v_1+v_{\text{w}})^2 + \frac{\eta\,T_1}{R} \tag{1}$$

where $m_{\text{eff}} = m + J/R^2$ is the effective mass, containing the mass of vehicle m, the moment of inertia J of the rotating elements, and the wheel radius R. Also, g is the gravitational constant, ϕ is the inclination angle, μ is the rolling resistance coefficient, b is the motor damping ratio, ν is the air drag constant, v_{w} is the velocity of the head wind, η is the gear ratio, and T_1 is the actuation torque.

To simplify the analysis, the vehicle is assumed to run on a flat road with no head wind, i.e., $\phi = 0$ and $v_{\text{w}} = 0$. In addition, the moment of inertia of the rotational parts is neglected, i.e., $J \approx 0$, which implies $m_{\text{eff}} \approx m$. We introduce the distance h_1 as the other state of the system, resulting in the overall dynamics

$$\begin{aligned} \dot{h}_1 &= v_0 - v_1 \\ \dot{v}_1 &= -\mu g - \frac{b}{m} v_1 - \frac{\nu}{m} v_1^2 + u_1 \end{aligned} \tag{2}$$

where u_1 is the desired acceleration given by the controller, and used to calculate the actuation torque T_1, that is,

$$T_1 = \frac{mR}{\eta} u_1. \tag{3}$$

The controller on the follower outputs the desired acceleration u_1 such that it should be able to regulate its velocity v_1 and the inter-vehicle distance h_1 based on the predecessor's velocity v_0.

In particular, the follower shall try to match its velocity v_1 to that of the predecessor v_0. However, if the predecessor's velocity exceeds the speed limit $v_{\max}$, the controller should switch from velocity matching to tracking with preset maximum velocity $v_{\max}$. This target velocity can be formulated as

$$W(v_0) = \begin{cases} v_0, & \text{if } v_0 < v_{\max} \\ v_{\max}, & \text{if } v_0 \geq v_{\max} \end{cases} \tag{4}$$

shown in Fig. 2(a).

On the other hand, the distance regulation typically involves a *range policy* $V(h_1)$, which gives the desired velocity as a function of the distance h_1. Although different range policies can be considered, they must satisfy the following requirements:

1) continuous and monotonously increasing (the more sparse traffic is, the faster the vehicles intend to run);
2) equal to zero for $h_1 \leq h_{\text{st}}$ (vehicles intend to stop within a safety distance);
3) equal to the speed limit for $h_1 \geq h_{\text{go}}$ (vehicles intend to run with a given maximum speed in sparse traffic—often referred to as *free flow*).

Here, we consider the range policy

$$V(h_1) = \begin{cases} 0, & \text{if } h_1 \leq h_{\text{st}} \\ \dfrac{v_{\max}}{h_{\text{go}} - h_{\text{st}}}(h_1 - h_{\text{st}}), & \text{if } h_{\text{st}} < h_1 < h_{\text{go}} \\ v_{\max}, & \text{if } h_1 \geq h_{\text{go}} \end{cases} \tag{5}$$

depicted in Fig. 2(b) that will be used throughout this paper. The reciprocal of the slope in the linear range

$$t_{\text{h}} = \frac{h_{\text{go}} - h_{\text{st}}}{v_{\max}} \tag{6}$$

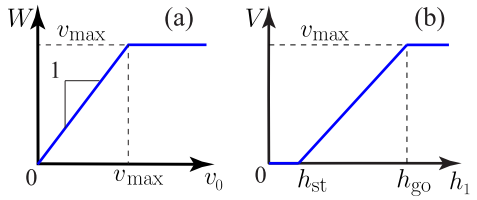

Fig. 2. (a) Saturation function (4). (b) Range policy function (5).

is often referred to as *time headway*. A smaller time headway may increase the traffic throughput if string stability is maintained. This will be discussed more in Section IV.

In order to match velocities and regulate inter-vehicle distance, we propose a controller to command the acceleration according to

$$\begin{aligned} u_1 &= \alpha(V(h_1) - v_1) + \gamma\, \varepsilon_1 + \beta(W(v_0) - v_1) \\ \dot{\varepsilon}_1 &= V(h_1) - v_1. \end{aligned} \tag{7}$$

Here, u_1 is the acceleration command provided to the actuator. $V(h_1) - v_1$ represents the error between the desired velocity $V(h_1)$ and the follower's velocity v_1, whereas $W(v_0) - v_1$ describes the velocity matching error between the target velocity $W(v_0)$ and the follower's velocity v_1. The first two terms constitute a proportional-integral controller to regulate the distance, whereas the last term regulates the velocity. We remark that the integral controller is used to guarantee that the vehicle can maintain desired safety distance provided by the range policy $V(h_1)$. Note that α and β are measured in [1/s], γ is measured in [1/s^2]. We also remark that, in practice, the controller (7) is digitally implemented on a microcontroller and physical limitations result in saturations. Those effects will be studied in Sections III–V.

The control algorithm (7) requires the quantities v_0, v_1, and h_1. On the one hand, they can be obtained using range sensors such as radar and lidar, which is the typical way of implementing ACC in the industry. On the other hand, they can also be obtained via wireless V2V communication that can be used to supplement sensory information. This leads to a CCC of the simplest kind. Although in real vehicles, sensory and communication-based information shall be fused before applying the controller, in this paper, we are more interested in connectivity-based controller. In particular, we emphasize the benefits of connectivity including low cost, high signal quality, and most importantly, being able to operate when the predecessor is beyond the line of sight.

III. Testbed Setup

In order to test the proposed controller (7) and study its implications on traffic flow, we utilize a scaled connected vehicle testbed, consisting of a group of ground robots shown in Fig. 3(a), which can mimic the longitudinal dynamics of vehicles. In this section, the mechanical structure, the ECS, and the control-related software design are explained in detail.

A. Mechanical Design and System Architecture

The mechanical components and structure of the robots are shown in Fig. 3(b) and (c). The robots are rear-wheel driven

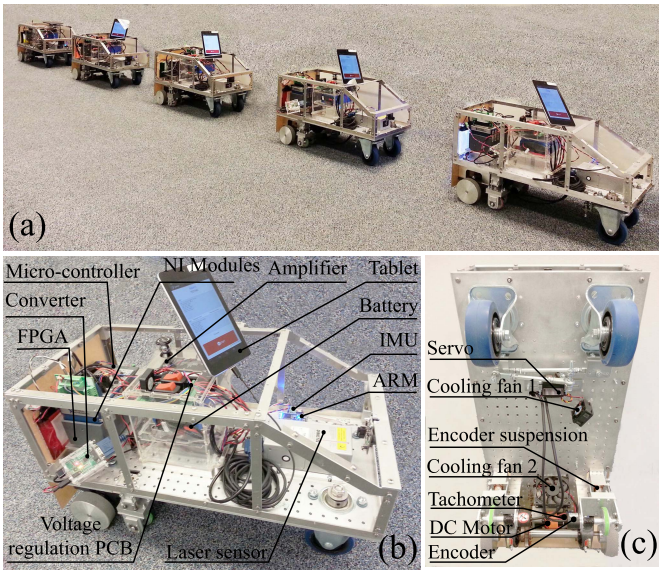

Fig. 3. (a) Group of ground robots. (b) Side view of a robot. (c) Bottom view of a robot.

TABLE I
SCALING FACTORS FROM REAL VEHICLES TO ROBOTS

length [m]	$1/8$
velocity [m/s]	$1/16$
time [s]	2
frequency [Hz]	$1/2$
acceleration [m/s^2]	$1/32$
control gain α [1/s]	1/2
control gain β [1/s]	1/2
control gain γ [1/s^2]	1/4

(without differential) by a brushed DC motor and front-wheel steered by a servo motor via an Ackermann steering system. To measure their position, the robots are equipped with an extra pair of mini-wheels with optical encoders. A suspension system ensures that those mini-wheels are always rolling on the ground.

Due to the characteristics of the hardware, safety concerns, and actuation capabilities, we scaled down the lengths and velocities by factors of 8 and 16, respectively. This results in the scaling factors given in Table I. For example, the time-scaling factor of 2 means that 200-ms V2V communication period on the robots corresponds to 100-ms period on the real-world vehicles. Similarly, the frequency-scaling factor of $1/2$ means that if the robot amplifies signals at frequency 0.15 Hz in the experiment, the vehicle with the corresponding controller will amplify signals at frequency 0.3 Hz in the real-world implementation. Table II shows the control parameters that we choose in (7) for real vehicles and robots based on the scaling. The remaining physical parameters of the robots are given in Table III.

Fig. 4 shows the functional block diagram of the ECS, consisting of power system, controllers, peripherals, sensors, and actuators. The power system includes a 24-V battery as the power supply and a printed circuit board (PCB) regulating multiple voltage levels for the sub-modules.

TABLE II
CONTROL PARAMETERS USED IN THE EXPERIMENTS

	Real Vehicles	Robots
$v_{\max}$ [m/s]	30	1.875
h_{st} [m]	5	0.625
h_{go} [m]	35	4.375
t_{h} [s]	1	2

TABLE III
PHYSICAL PARAMETERS OF THE ROBOTS

mass of the robot m [kg]	20.2
rear wheel radius R [m]	0.045
gear ratio η	$55/18$
air drag coefficient ν [kg/m]	0 (neglected)
damping ratio b [kg/s]	0 (neglected)
rolling resistance coefficient μ	0.008

An 800-MHz microcontroller handles all the sensor data post-processing, high-level controller computation, and data logging. It also communicates with a field-programmable gate array (FPGA) that is connected to the peripherals through different modules and enables data encoding, decoding, and processing at the exact time instants. An additional advance RISC machine (ARM) is utilized to pre-process data and communicate with sensors via serial peripheral interface (SPI) and inter-integrated circuit (I2C) protocols.

Each robot is equipped with an Android tablet to enable wireless communication with other robots. In particular, a mobile *ad hoc* network (MANET), capable of communicating over about 100-m range with very low rate of packet losses, is created to mimic V2V communication. The tablet communicates with the microcontroller through a USB to universal asynchronous receiving and transmitting (UART) converter and an Android application is designed to serve as human–machine interface (HMI).

A laser range sensor, two optical encoders, and a tachometer are used to measure the inter-robot distance, the distance traveled, and the angular velocity of the DC motor, respectively. Since the tachometer is attached to the motor shaft, the angular velocity is proportional to the longitudinal velocity of the robot with the assumption that the rear wheels do not slip.

A servo motor steers the front wheels for lateral control, whereas a brushed DC motor serves as the longitudinal actuator. Since the output torque of a brushed DC motor is proportional to the current on the motor windings, a servo amplifier is set in current mode to amplify the control signals and drive the DC motor. Also, since the current on the motor windings tracks the commanded current well, the output torque T_1 is equal to the commanded torque that is proportional to the commanded acceleration u_1 given in (7) [see (3)].

B. Control-Related Software Design

Here, we briefly discuss some control-related problems, i.e., clock synchronization, digital effects and delays, control loop alignment, and data processing.

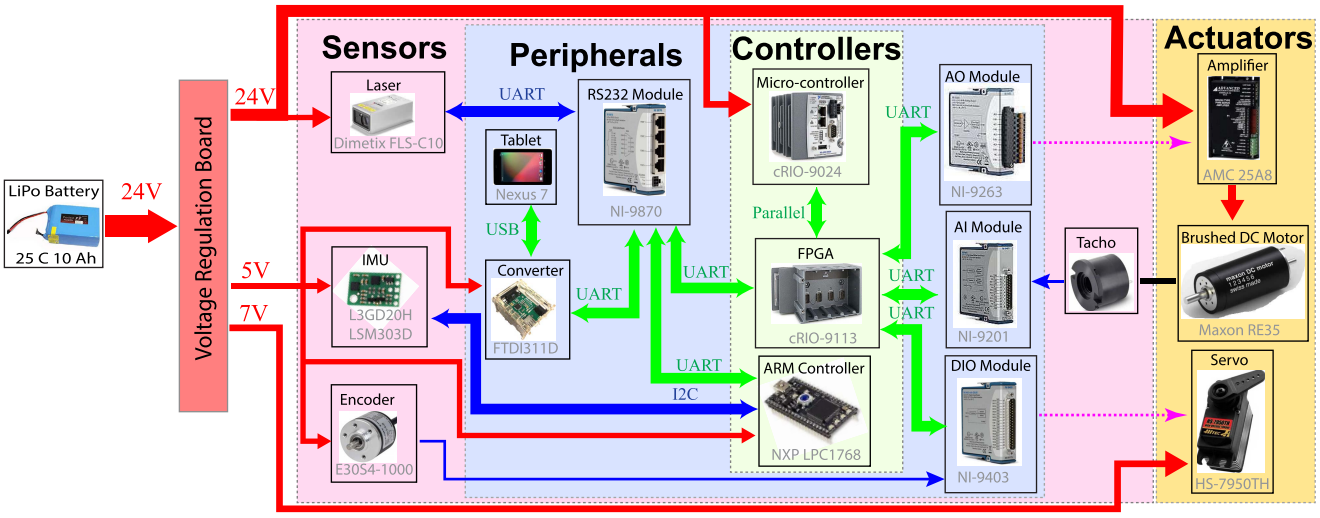

Fig. 4. Functional block diagram of a robot.

In a multi-agent system, clock synchronization plays an important role in analyzing the time-critical effects and data processing. To allow the maximum capacity in V2V communication networks, dedicated short range communication (DSRC) devices broadcast messages in a distributed manner within each sampling period to avoid channel congestion. Precision time protocol (PTP) [67] is often used to synchronize clocks among GPS and DSRC devices with sub-microseconds accuracy. In our experiments, instead of PTP, we exploit simple network time protocol (SNTP) [68], [69] to achieve clock synchronization with milliseconds accuracy.

Since DSRC devices broadcast messages at 10 Hz [70] with milliseconds latency [71], digital effects and delays arising from intermittency and packet drops impact the performance of the controllers. As control commands are updated periodically and kept unchanged in between, infrequent data exchange increases the delay in the control system and amplifies digital effects. The following definitions are proposed to facilitate the challenges caused by delays in communication-based control.

Definition 1: Communication delay is the time elapsed from the instant when the transmitter samples the physical data to the instant when the data are available to the receiver.

Definition 2: Information delay is the time elapsed from the instant when the transmitter samples the physical data to the instant when the data are used by the controller on the receiver.

In general, both delays can be non-deterministic due to the stochastic nature in V2V communication. However, in order to ensure the repeatability of the experiments, it is desirable to have some determinism. In Appendix A, we provide details how we guarantee that the information delay remains constant while the communication delay varies stochastically. The key points are summarized as follows.

The communication delay is intrinsic and cannot be changed, resulting in the fact that the information about the transmitter is not immediately available to the receiver. However, from the control perspective, one cares about how much information delay has been aggregated before the controller utilizes the data. Moreover, it is shown that the range where communication delay varies is much smaller than the control period based on V2V communication. By aligning the starting time of control loops on different robots sufficiently accurately, the information about the transmitter at the current control period can be available to the receiver before the start of its next control period. Indeed, this may also be realized on real vehicles with DSRC devices. The following analysis on digital effects and delays are based on this assumption.

Last but not least, filtering also needs to be considered in the controller design. In order to get cleaner sensory data, filters/observers, which utilize information of the previous few steps to get a better estimate of the current step, are needed. Delays appear in this process, which depend on the period of sensory data processing loop. In order to eliminate this problem, the sensory data processing loop is set to be much faster than the control loop.

The values of the timing errors in our testbed are given in Table V in Appendix B. Indeed, they are orders of magnitude smaller than the period in V2V communication, which typically has the order of hundreds of milliseconds. The accuracy in timing lays a solid foundation for the study of digital effects, delays, and stability in the rest of this paper.

IV. Modeling and Analysis

In this section, we derive the closed-loop dynamics when applying the controller (7) with the digital implementation based on the setup in Section III. Subsequently, linearization and discretization are carried out for further analysis. Stability diagrams are used to summarize the results.

A. Closed-Loop Dynamics

According to Section III-B, the follower synchronizes its clock and aligns its control loop with the predecessor's. We assume that the kinematic information is sampled and broadcast intermittently with sampling time Δt, resulting in the time mesh $t_k = k\Delta t$, $k = 0, 1, 2, \ldots$ [see Fig. 5(a)].

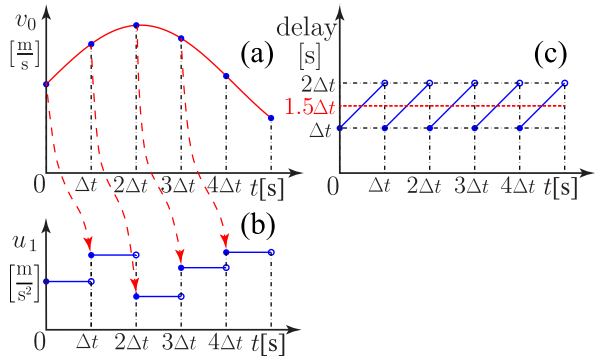

Fig. 5. (a) Sampling. (b) Control with ZOH. (c) Delay variations.

At time instant t_k, the information available to the follower is the state of the predecessor measured at t_{k-1}. Thus, the controller on the follower outputs a control command at t_k based on the information about the predecessor at t_{k-1} and keeps it constant until the next updating instant t_{k+1}, which is known as zero-order hold (ZOH) [see Fig. 5(b)]. This means that the effective delay increases from Δt to $2\,\Delta t$ during each control interval as shown in Fig. 5(c), resulting in the average delay $1.5\,\Delta t$. Note that the physical part of the model still evolves in continuous time. Thus, the digitally controlled system can be written as

$$\begin{aligned}\dot{h}_1 &= v_0 - v_1\\ \dot{v}_1 &= -\mu\, g - \frac{b}{m} v_1 - \frac{\nu}{m} v_1^2\\ &\quad + \alpha(V(h_1(t_{k-1})) - v_1(t_{k-1})) + \gamma\, \varepsilon_1(t_k)\\ &\quad + \beta(W(v_0(t_{k-1})) - v_1(t_{k-1})), \quad t_k \le t < t_{k+1}\\ \varepsilon_1(t_k) &= \varepsilon_1(t_{k-1}) + (V(h_1(t_{k-1})) - v_1(t_{k-1}))\,\Delta t. \end{aligned} \tag{8}$$

Note that the third equation in (8) represents digital implementation of the integral controller.

For $v_0 \le v_{\max}$, system (8) possesses the equilibrium

$$v_1^* = v_0^* = V(h_1^*), \quad \varepsilon_1^* = \frac{1}{\gamma}\left(\mu\, g + \frac{b}{m} v_1^* + \frac{\nu}{m}(v_1^*)^2\right). \tag{9}$$

When extended to longer vehicle chains, this is often referred to as the *uniform flow equilibrium* as vehicles travel with the same velocity while keeping the desired distance.

For simplicity, we linearize the system about the equilibrium (9). With the definition of perturbations

$$\begin{aligned}\tilde{h}_1 &= h_1 - h_1^*, \quad \tilde{v}_1 = v_1 - v_1^*\\ \tilde{\varepsilon}_1 &= \varepsilon_1 - \varepsilon_1^*, \quad \tilde{v}_0 = v_0 - v_0^* \end{aligned} \tag{10}$$

we obtain

$$\begin{aligned}\dot{\tilde{h}}_1 &= \tilde{v}_0 - \tilde{v}_1\\ \dot{\tilde{v}}_1 &= -c\,\tilde{v}_1 + \frac{\alpha}{t_{\mathrm{h}}}\tilde{h}_1(k-1) + \beta\,\tilde{v}_0(k-1)\\ &\quad - (\alpha+\beta)\,\tilde{v}_1(k-1) + \gamma\,\tilde{\varepsilon}_1(k), \quad t_k \le t < t_{k+1}\\ \tilde{\varepsilon}_1(k) &= \tilde{\varepsilon}_1(k-1) + \frac{\Delta t}{t_{\mathrm{h}}}\tilde{h}_1(k-1) - \Delta t\,\tilde{v}_1(k-1) \end{aligned} \tag{11}$$

where

$$c = \frac{b + 2\,\nu\, v_1^*}{m} \tag{12}$$

and the shorthand notation $\tilde{h}_1(k) = \tilde{h}_1(t_k)$, $\tilde{v}_1(k) = \tilde{v}_1(t_k)$, $\tilde{\varepsilon}_1(k) = \tilde{\varepsilon}_1(t_k)$, and $\tilde{v}_0(k) = \tilde{v}_0(t_k)$ is introduced.

Based on Fourier's theory, periodic signals can be represented as a countable sum of sines and cosines, which can also be extended to absolutely integrable aperiodic signals using Fourier transform. Henceforth, we assume sinusoidal variations in the predecessor's velocity, that is,

$$v_0(t) = v_0^* + v_0^{\mathrm{amp}} \sin(\omega\, t) \implies \tilde{v}_0(t) = v_0^{\mathrm{amp}} \sin(\omega\, t) \tag{13}$$

where v_0^{amp} and ω are the amplitude and angular frequency of the fluctuations in the predecessor's velocity. Solving the system (11), one can obtain

$$\begin{aligned} X(k+1) &= \mathbf{A}\, X(k) + \mathbf{B}\, U(k)\\ Y(k) &= \mathbf{C}\, X(k) \end{aligned} \tag{14}$$

where the state, input, and output are given by

$$X(k) = \begin{bmatrix} \tilde{h}_1(k)\\ \tilde{v}_1(k)\\ \tilde{\varepsilon}_1(k)\\ \tilde{h}_1(k-1)\\ \tilde{v}_1(k-1) \end{bmatrix}, \quad U(k) = \begin{bmatrix} \tilde{v}_0(k)\\ \tilde{v}_0^{\perp}(k) \end{bmatrix}, \quad Y(k) = \tilde{v}_1(k) \tag{15}$$

and

$$\tilde{v}_0^{\perp}(t) = v_0^{\mathrm{amp}} \cos(\omega\, t). \tag{16}$$

The matrices $\mathbf{A}$, $\mathbf{B}$, and $\mathbf{C}$ are provided in (42) in Appendix C. Note that the scalar sinusoidal input (13) for the continuous-time system (8) results in the vector-valued input (15) for the discrete-time system (14) despite their dependent nature.

B. Plant Stability and String Stability

To check plant stability, we analyze the linearized system (14). For plant stability of nonlinear systems, we refer the reader to [56]. Without disturbances on the predecessor's velocity, i.e., $v_0^{\mathrm{amp}} = 0$ in (13, 16) or $U(k) = 0$ in (15), the linearized system (14) simplifies to a linear autonomous map. The local asymptotic stability of the uniform flow equilibrium (9) of the system (8) is equivalent to the asymptotic stability of the origin of the linear autonomous map. Thus, the system (8) is locally plant stable if all the eigenvalues of the matrix $\mathbf{A}$ in (14) are within the unit circle in the complex plane. These eigenvalues $z \in \mathbb{C}$ are given by the characteristic equation

$$\det(z\,\mathbf{I} - \mathbf{A}) = 0 \tag{17}$$

where $\mathbf{I} \in \mathbb{R}^{5\times 5}$ is the identity matrix. Bisection method explained in [53] can be used to trace the boundaries in the parameter space $(\alpha, \beta, \gamma, \Delta t, t_{\mathrm{h}})$.

Fig. 6 shows the plant stability diagram in the (β, α)-plane for the robot with the parameters given in Table II for different sampling time Δt and γ gains. The red curves correspond to plant stability boundaries while the shaded regions enclosed by them are plant stable domains. Fig. 6 illustrates that the

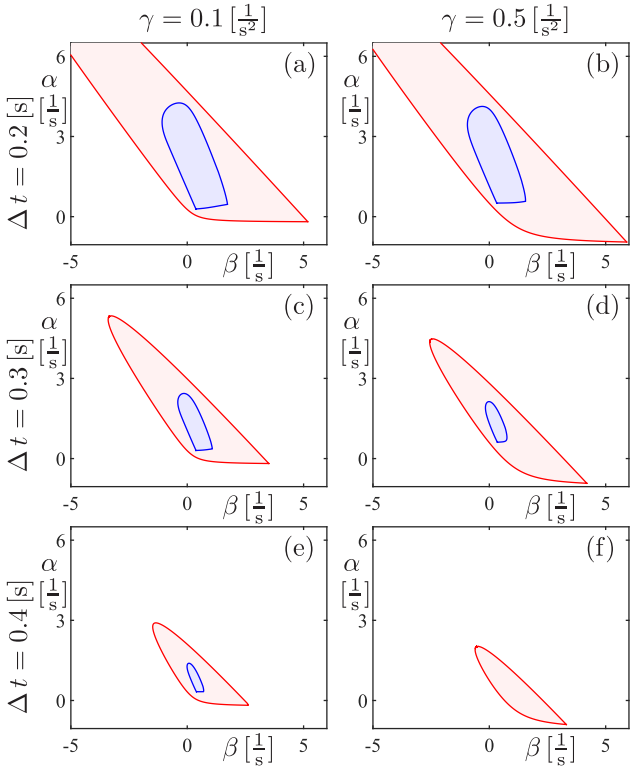

Fig. 6. Stability diagrams. The red curves and the enclosed shaded regions are the plant stability boundaries and plant stable domains, respectively, whereas the blue curves and the shaded blue regions are the string stability boundaries and string stable domains, respectively.

plant stable domains shrink as the sampling time Δt increases, i.e., it will be harder to design controllers for larger sampling time. On the other hand, changing the integral gain γ does not affect plant stability significantly except a slight shift in the stability domains.

To analyze string stability, we again focus on the linearized system (14). With the assumption that the disturbances have finite energy and are absolutely integrable, disturbance attenuation is equivalent to the attenuation of sinusoidal perturbations at all frequencies according to Fourier's theory and superposition principle of linear systems. In other words, string stability is achieved when the amplification ratio in the velocity fluctuations is less than 1 for all frequencies. From the linear system theory, this amplification ratio can be obtained through transfer functions.

The contributions of the two dependent inputs $\tilde{v}_0(k)$ and $\tilde{v}_0^{\perp}(k)$ in (14) have to be summed up when deriving the output $\tilde{v}_1(t)$. Applying Z transform to (14), we can obtain the amplification ratio and phase lag as

$$M(\omega) = |\Gamma(e^{j\omega\,\Delta t})|, \quad \psi(\omega) = \angle\,\Gamma(e^{j\omega\,\Delta t}) \tag{18}$$

where the transfer function is given by

$$\Gamma(z) = \mathbf{C}(z\,\mathbf{I} - \mathbf{A})^{-1}\mathbf{B}\mathbf{E} \tag{19}$$

and

$$\mathbf{E} = [1 \quad j]^{\top} \tag{20}$$

is used to sum up the effects of two dependent inputs [53]. We remark that the vector $\mathbf{E}$ is obtained in the same way as in [53] by calculating the amplification ratio and phase lag of the steady-state output to the input using trigonometric identities and Euler's formula. Thus, the condition for string stability is given by

$$\sup_{\omega>0} M(\omega) < 1. \tag{21}$$

Note that M also depends on the parameters $(\alpha, \beta, \gamma, \Delta t, t_h)$. Similar to the plant stability boundaries, the bisection method is used to trace the string stability boundaries.

In Fig. 6, the blue curves denote the string stability boundaries and the shaded light blue regions are string stable. We remark that there are string stable domains outside the plant stable domains that are not shown in the figure. As the sampling time Δt increases, string stable domains shrink and finally disappear after exceeding the critical value Δt_{cr}, i.e., it is getting harder and finally impossible to choose gains that can ensure string stability of the system. It is shown in [59] that

$$\Delta t_{cr} \approx \frac{1}{3}\,t_h. \tag{22}$$

This implies that when the V2V communication period Δt is fixed, to ensure string stability, the driver selected time headway t_h must satisfy

$$t_h \gtrapprox 3\Delta t. \tag{23}$$

Moreover, comparing the columns shown in Fig. 6, we see that varying the integral gain γ may significantly influence string stability. This is because the integral controller is used only to maintain the desired equilibrium (9), and large integral gains will destabilize the system. One may also note that the string stable domains shown in Fig. 6 also covers part of the second quadrant, implying that negative β might be used when α is large enough. This is because, in the presence of large α, vehicle is very responsive to the changes in the distance regulation error [see (7)]. Thus, the system can tolerate the improper design in velocity regulation (negative β). However, we remark that, in practice, gains should be chosen in the string stable domain in the first quadrant to achieve the best performance.

V. Experiments With Two Robots

To validate the theoretical results in Section IV, we conduct a set of experiments with two robots for the predecessor-follower system. First, the data resources are explained. Then, the major concerns in tracing the experimental string stability boundaries are discussed, followed by the test procedure. Finally, the results are illustrated to show the correspondence between the theoretical analysis and experimental outcomes.

When applying the controller (7), the follower needs to access its own velocity v_1, the inter-vehicle distance h_1, and the predecessor's velocity v_0. The tachometer and the encoders on each robot can measure its own velocity and position, respectively. Moreover, the predecessor broadcasts its position s_0 and velocity v_0 through V2V communication. Thus, the inter-vehicle distance

$$h_1 = s_0 - s_1 - l \tag{24}$$

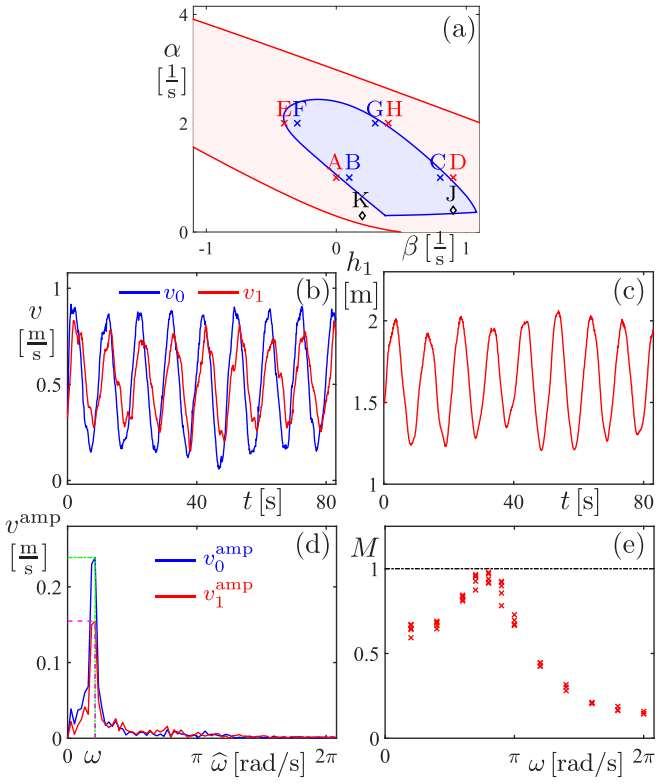

Fig. 7. Experiment procedure. (a) Stability diagram for $\Delta t = 0.3$ [s] and $\gamma = 0.1$ [1/s^2]. (b) and (c) Typical profiles in an experiment. (d) FFT results of the velocity profiles. (e) Experimental amplification ratios at different frequencies.

is calculated on the follower's microcontroller, where s_1 is the follower's position and l is the follower's length (see Fig. 1).

To validate whether the proposed analytical method can capture the major phenomena caused by digital effects and delays in V2V communication, a set of experiments is conducted to validate the stability boundaries experimentally. For safety reasons, only string stability is tested. Physical limitations are taken into account to avoid saturations as such nonlinearities are out of the scope of this research. First, we set the saturation limits as high as possible while still ensuring the proper protection of the hardware. Thus, the allowable acceleration of the robots is in the interval $[-a_{\max}, a_{\max}]$ with $a_{\max} \approx 0.72$ [m/s^2]. Then, we select parameters that can prevent the robots from reaching the saturation point. The sampling interval is chosen to be $\Delta t = 0.3$ [s], resulting in a practical feasible string stable region with reasonable gains [see Fig. 7(a)]. Finally, the amplitude of the oscillations v_0^{amp} in the predecessor's velocity is chosen to make the noise negligible while ensuring that neither the predecessor nor the follower reaches the acceleration limit $a_{\max}$. That is, according to (13, 18), we require

$$\omega v_0^{\text{amp}} \le a_{\max}, \quad \omega v_0^{\text{amp}} M(\omega) \le a_{\max}. \tag{25}$$

To validate the theoretical string stability boundaries, we run tests corresponding to the points marked as A–H in Fig. 7(a) (points J and K will be discussed in Section VI). During each test, the predecessor introduces a sinusoidal excitation signal (13) at frequency ω into the system with the amplitude satisfying conditions (25). For case C, the time profiles of the resulting velocity and inter-vehicle distance are shown in Fig. 7(b) and (c) for frequency $\omega = 0.2\,\pi$ [rad/s] and $v^* = 0.5$ [m/s], respectively. By applying fast Fourier transform (FFT) to the velocities, the amplitude can be obtained as shown in Fig. 7(d), and the experimental amplification ratio is calculated as

$$M_{\text{exp}}(\omega) = \frac{v_1^{\text{amp}}(\omega)}{v_0^{\text{amp}}(\omega)} \tag{26}$$

corresponding to a red cross shown in Fig. 7(e). Through the repetition of the above-mentioned process, an experimental frequency response with mean value and error bar can be generated, and this may be repeated for different ω frequencies. In this way, the string stability boundary can be validated experimentally.

In order to quantify the mismatches between theoretical and experimental results, *relative error percentage* is defined as

$$e_{\text{M}}(\omega) = \left| \frac{\bar{M}_{\text{exp}}(\omega) - M(\omega)}{M(\omega)} \right| \tag{27}$$

where $\bar{M}_{\text{exp}}(\omega)$ is the mean value of the experimental amplification ratios at the given frequency ω.

Since the frequencies with relatively larger amplification ratios are more critical when determining experimental string stability, we define the *maximum critical error percentage* as

$$\hat{e}_{\text{M}} = \max_{\omega \in \Omega} e_{\text{M}}(\omega). \tag{28}$$

Here, Ω is a subset of the tested frequencies Ω_{test} corresponding to high enough amplification ratios, that is,

$$\Omega = \{\omega \in \Omega_{\text{test}} \,|\, M(\omega) > M_{\text{crit}}\}. \tag{29}$$

The error for phase lags can be defined in a similar way.

In order to validate the experimental string stability boundaries, we present here the results of CCC experiments for the gain combinations marked as A–H in Fig. 7(a) (see Appendix D for the corresponding numerical values).

Fig. 8 shows the resulting amplification ratios for different cases. The red solid curves represent the theoretical results, whereas the blue crosses with error bars denote the experimental outcomes. As illustrated, the experimental amplification ratios match pretty well with the theoretical ones. We remark that similar results can be observed for phase lags but are not shown here to avoid repetition. In other words, the theoretical analysis in Section IV is able to capture the major dynamics and the results indicate that string stability can be achieved experimentally in the presence of relative large information delay. Finally, we list the maximum critical error percentages for all the experiments in Table IV when $M_{\text{crit}} = 0.5$ [see (27)–(29)].

VI. Experiments With Multiple Robots

In this section, to demonstrate how string stable CAVs improve traffic performance, experiments are conducted using five robots where each robot controls its motion based on its own predecessor's information. First, we show the overall

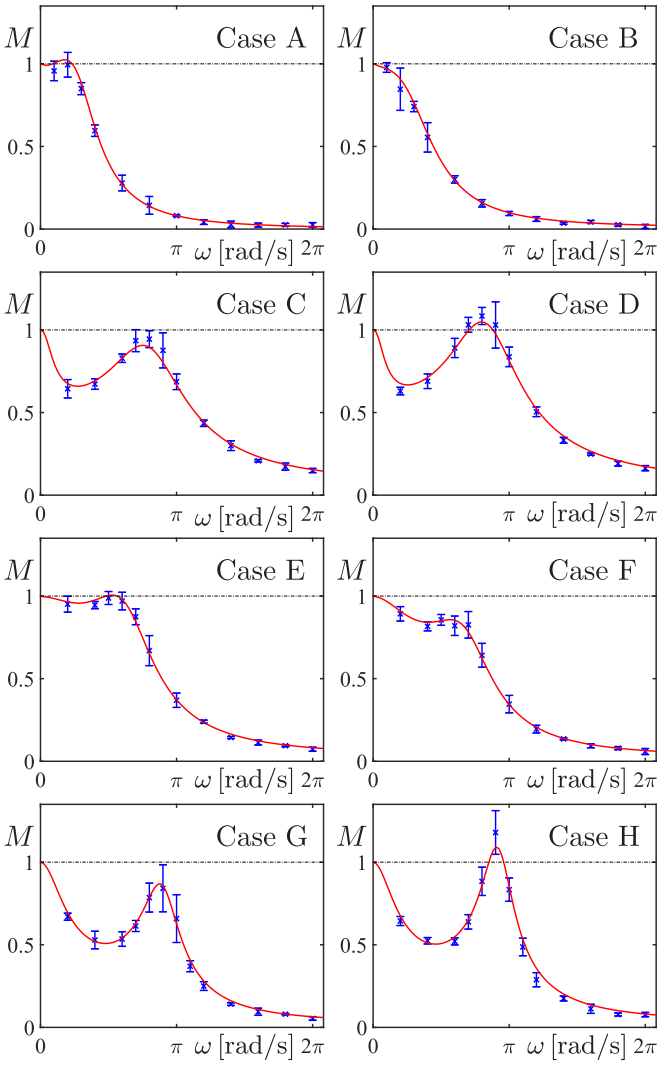

Fig. 8. Amplification ratios as a function of excitation frequency. Red curves: theoretical results. Blue error bars: experimental results of two-car CCC.

performance of a chain of string unstable vehicles and a chain of string stable vehicles, respectively. Then mixed chains of string stable and string unstable vehicles are studied to evaluate the impact of different penetration rates on traffic dynamics.

In Section V, experiments showed a satisfactory correspondence with the theoretical results. Here, two sets of gains are chosen corresponding to points K and J on the stability diagram shown in Fig. 7(a). The theoretical amplification ratios for cases K and J are shown in Fig. 9. Vehicles using gains corresponding to case K are referred to as string unstable, whereas those gains corresponding to case J are referred to as string stable from now on. Previous research showed that human drivers exhibit string unstable behaviors due to large reaction delay and inaccurate sensing [72]. In Appendix E, we present the estimated parameters for the model in [72], and compare the frequency responses against that of case K (by taking into account the scaling). Similar responses imply that the settings of case K can mimic human driving behaviors in terms of string instability.

In the following experiments, the frequency $\omega_0 = 0.15\,\pi$ [rad/s] highlighted in Fig. 9 is used as the excitation frequency

TABLE IV
MAXIMUM CRITICAL ERROR PERCENTAGE

maximum critical error percentage	amplification ratio	phase lag
case A	4.6%	14.0%
case B	6.7%	17.7%
case C	9.0%	6.4%
case D	6.8%	7.1%
case E	3.6%	4.5%
case F	5.6%	3.3%
case G	4.9%	7.5%
case H	8.7%	3.3%

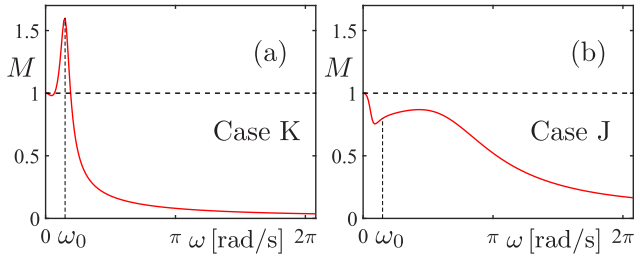

Fig. 9. Amplification ratio as a function of excitation frequency.

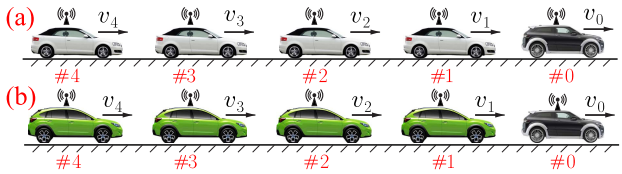

Fig. 10. (a) Four string unstable vehicles follow a head vehicle. (b) Four string stable vehicles follow a head vehicle.

for periodic fluctuations, and we set $v_0^* = 0.75$ [m/s]. Also, we use white and green vehicles to represent string unstable vehicles for case K and string stable vehicles for case J, respectively. The black vehicle is used to represent the head vehicle that introduces velocity fluctuations (see Figs. 10 and 14).

First, we demonstrate how string unstable vehicles amplify fluctuations in traffic flow using the configuration shown in Fig. 10(a) where the following four vehicles are all string unstable. Fig. 11 shows the velocity profiles for periodic excitations of different sizes. One can see that the fluctuations are gradually amplified along the chain for all the cases, and full stops may be reached when the amplified fluctuations are large enough.

In practice, excitations are typically not periodic but contain signals of different frequencies. Thus, fluctuations at frequencies with amplification ratio larger than 1 are amplified while those at other frequencies are attenuated. To demonstrate this phenomenon, another set of experiments is conducted where the head vehicle generates aperiodic velocity excitations and the results are shown in Fig. 12 for different sizes of perturbations. It can be seen that perturbations are amplified as propagating along the vehicle chain and full stops are also reached for large enough perturbations.

Figs. 11 and 12 also show that the amplification phenomena are similar regardless of the sizes of perturbations. In the experiments, we would like to distinguish signals from

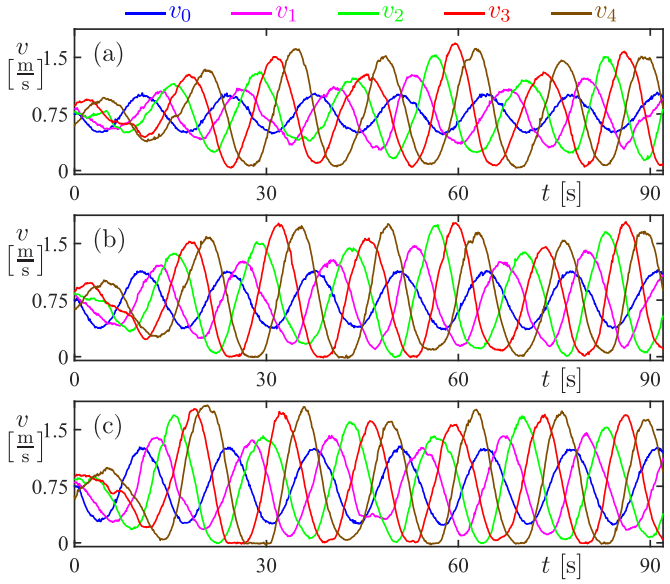

Fig. 11. Responses to periodic excitations with four string unstable vehicles configured as shown in Fig. 10(a). (a) $v_0^{\text{amp}} = 0.25$ [m/s]. (b) $v_0^{\text{amp}} = 0.375$ [m/s]. (c) $v_0^{\text{amp}} = 0.5$ [m/s].

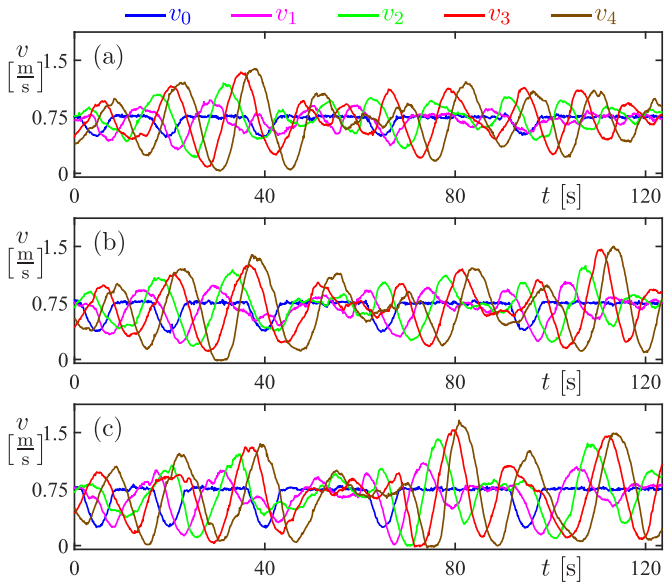

Fig. 12. Responses to aperiodic excitations with four string unstable vehicles configured as shown in Fig. 10(a). (a) $v_0^{\text{amp}} = 0.25$ [m/s]. (b) $v_0^{\text{amp}} = 0.375$ [m/s]. (c) $v_0^{\text{amp}} = 0.5$ [m/s].

sensor noises, so velocity variations with larger amplitude are preferred. Also, saturation in the velocities should be avoided, since it affects amplification ratio. Thus, in the following experiments, we choose a particular excitation size to meet the requirements above. More specifically, if the following vehicles attenuate velocity fluctuations, a larger perturbation is applied on the first vehicle so that the following vehicles' signals are distinguishable from noises. On the contrary, if the following vehicles are amplifying fluctuations, a smaller variation is imposed on the first vehicle so that the following vehicles do not saturate.

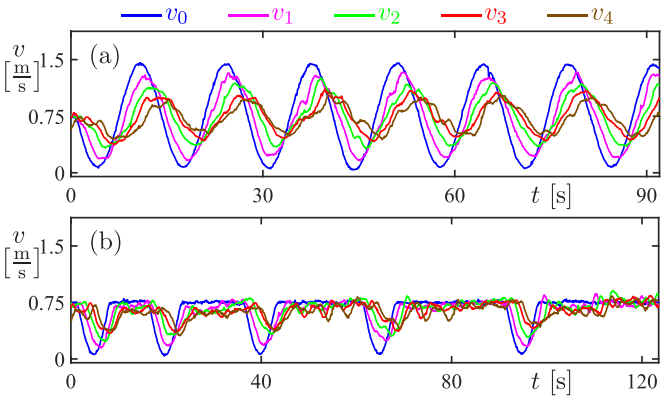

Fig. 13. Responses to excitations with four string stable vehicles configured as shown in Fig. 10(b). (a) Periodic excitation. (b) Aperiodic excitation.

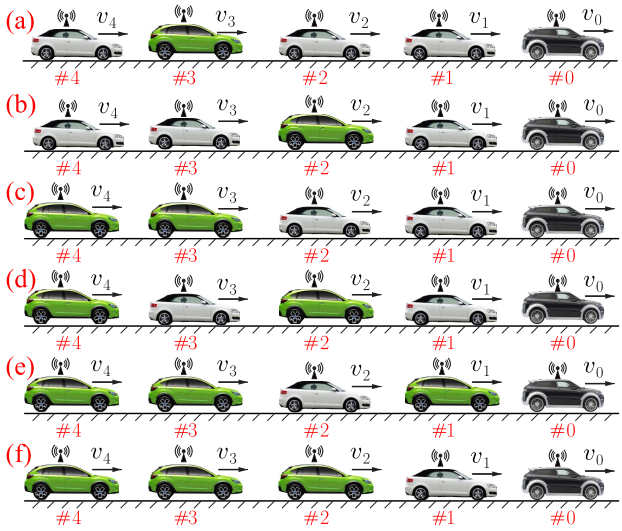

Fig. 14. Vehicle configurations for different penetration rates of string stable vehicles (green) among string unstable vehicles (white). (a) and (b) One string stable vehicle. (c) and (d) Two string stable vehicles. (e) and (f) Three string stable vehicles.

In order to show how string stable vehicles attenuate fluctuations in traffic flow, we use the configuration shown in Fig. 10(b) where the following four vehicles are all string stable. The corresponding velocity profiles for periodic and aperiodic excitations are shown in Fig. 13(a) and (b), respectively. They indicate that a chain of string stable vehicles is able to attenuate oscillations introduced by the head vehicle. In Fig. 13(b), tiny velocity fluctuations are still observable in the following vehicles when the velocity of the head vehicle is almost constant. This is caused by the disturbances in the road grade variations, steering efforts, measurement noise, and so on.

Comparing the results between Figs. 11 and 13(a), or those between Figs. 12 and 13(b), one can see the differences are significant depending on whether the vehicles in the chain are string stable or not. In the remainder of this section, we study the behaviors for mixed chains of string stable and string unstable vehicles. String unstable vehicles are used to mimic the behaviors of human drivers, whereas string stable vehicles represent CCC vehicles. Fig. 14 depicts different

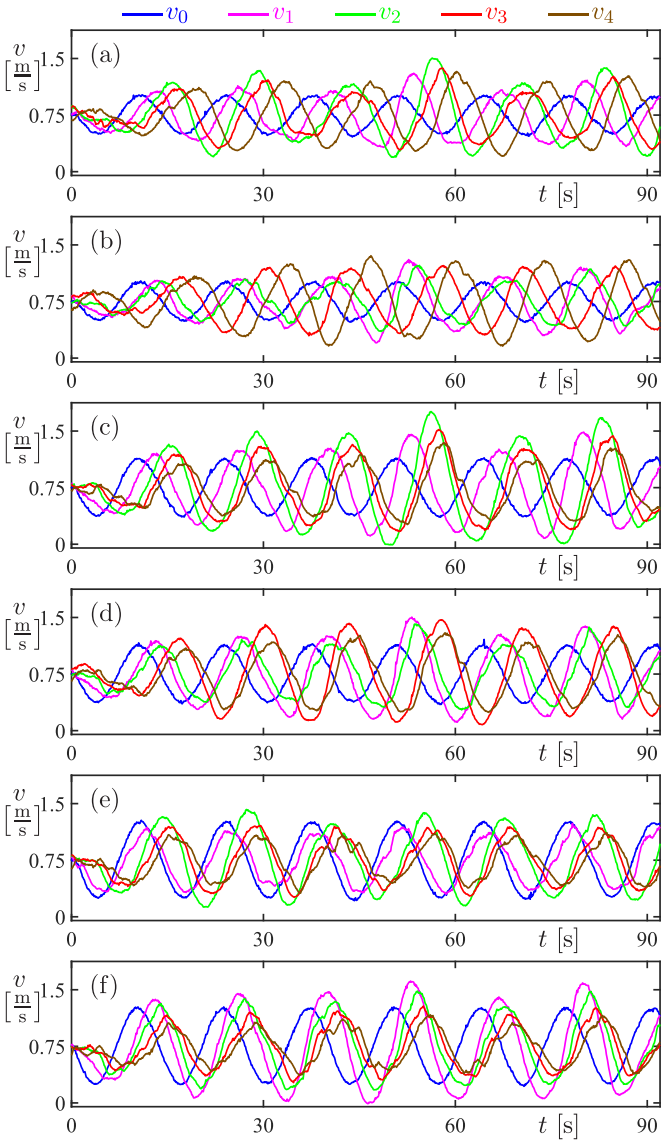

Fig. 15. Responses to periodic excitations as the penetration rate of string stable vehicle varies.

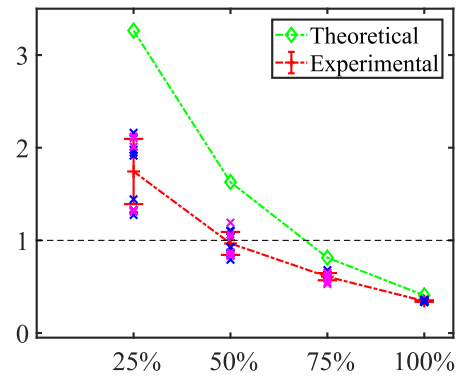

Fig. 16. Amplification ratio versus penetration rate of string stable vehicles.

configurations where out of the following four vehicles, one, two, and three of them are set to be string stable to represent 25%, 50%, and 75% penetration rates, respectively. Indeed, there are $2^4 = 16$ different configurations, but only two of them will be demonstrated for each penetration rate when there exists multiple.

Fig. 15 shows the corresponding velocity profiles for the configurations depicted in Fig. 14. In Fig. 15(a) and (b), with only one string stable vehicle in the chain, the oscillation amplitude of v_4 is much larger than that of v_0. However, as the number of string stable vehicles increases, the amplification of fluctuations becomes weaker as illustrated in Fig. 15(c) and (d) where two string stable vehicles are included. Fig. 15(e) and (f) indicates that the fluctuations can be attenuated when the number of string stable vehicles reaches three. Note that the difference in the amplification ratio from the head to the tail for the same penetration rate is negligible when comparing the results between (a) and (b), (c) and (d), or (e) and (f).

To quantify the phenomena mentioned above, each test is repeated multiple times for all the configurations shown in Fig. 14. After each test, FFT was used to obtain the amplification ratio from the head vehicle to the tail vehicle at the frequency ω_0 as discussed in Section V. As explained in Section II, the connectivity structure of CAVs motivates us to study head-to-tail string stability. The results are summarized in Fig. 16. The blue and magenta crosses for the same penetration rate represent the results of two different configurations. One can see that their experimental distributions are similar regardless of the difference in configurations. Thus, they are treated equally when calculating the mean value and standard deviation of the experimental amplification ratios, which are represented by the dashed red curve with error bars. The dashed green curve with diamond markers represents the theoretical amplification ratio at the same frequency. The mismatches between the experimental and theoretical results at low penetration rates are mainly caused by the actuator limitations and nonlinear effects in the presence of large oscillations. The results indicate that when the penetration rate of string stable vehicles exceeds 50% fluctuations can be attenuated in our experiments.

VII. Conclusion

In this paper, we investigated the dynamics of connected vehicle systems experimentally with the help of a scaled experimental testbed consisting of ground robots. We designed a predecessor-follower controller and tested it using CCC based on V2V communication. By modeling the longitudinal dynamics of the robots and incorporating digital effects and time delays in the control loops, we derived the theoretical stability diagrams for plant stability and string stability and verified them experimentally using a two-robot system. This way we demonstrated the validity of model-based design and showed that the V2V communication-based control can achieve the desired performance.

In order to investigate the scalability of CCC to larger traffic systems, we conducted a set of experiments with five robots. We demonstrated that when all vehicles are string unstable, fluctuations keep increasing as they propagate backward along the chain of vehicles and may even lead to full stops. On the contrary, when all vehicles are string stable, the fluctuations

decay leading to smooth traffic flow. In mixed traffic scenarios containing both string stable and string unstable vehicles, our experiments showed that a high enough penetration rate of the former type of vehicles may attenuate fluctuations and smooth out the ripples in traffic. This suggests that having high penetration rate of connectivity with appropriately designed automation, indeed, can impact traffic positively.

We remark that the advantages of connectivity are only partially exploited in the experiments in this paper since each follower only utilizes the information of its direct predecessor. In order to maximize the benefits of V2V communication, in a follow-up paper, we will experimentally demonstrate that CCC may improve traffic performance at low penetration rates of automation when utilizing motion information from multiple vehicles ahead.

APPENDIX

A. Control Loop Alignment

In this section, we explain communication-based control in detail and the way to ensure that the information delay is deterministic and quantitatively measurable by aligning the control loops of multiple robots.

Let us consider the scenario where the controller of robot 1 uses the information of robot 0 obtained from wireless communication. Fig. 17 shows two different cases in control loop timing between robot 0 and 1. The horizontal axes are the timelines of different robots, whereas the color boxes represent different tasks/threads as explained in the legend at the top. One may note that there might be several tasks/threads running at the same time, which is possible in multi-threading control systems.

As illustrated, to transceive data via wireless communication, a sequence of tasks should be performed on the transmitter, that is, sampling, processing (including converting from raw sensor data to physical data and filtering or estimation), and encoding according to the communication protocol before transmission. Upon the arrival of the transmitted data, the receiver decodes the data based on the protocol, and the information about the transmitter is updated and ready to be used in the receiver. This communication delay $\Delta_c(k)$ varies among different periods, devices as well as data rates. With the assumption that $\Delta_c(k)$-s are independently, identically distributed at each step, we transceived about 7000 packets in the experiment and plot the resulting histogram of communication delay shown in Fig. 18(a), which is close to a gamma distribution indicated by the red curve.

Fig. 17(a) shows a scheme of three control cycles with period Δt (the same as wireless communication period) when the control loops of robots 0 and 1 are not aligned, i.e., there is an alignment error

$$\Delta_A(k) = t(k^{(1)}) - t(k^{(0)}) \tag{30}$$

where $t(k^{(0)})$ and $t(k^{(1)})$ represent the closest two time instants correspond to $t(k)$ on robot 0 and 1, respectively. Note that this alignment error depends highly on the time difference when the controllers first start on different robots, but vaguely on

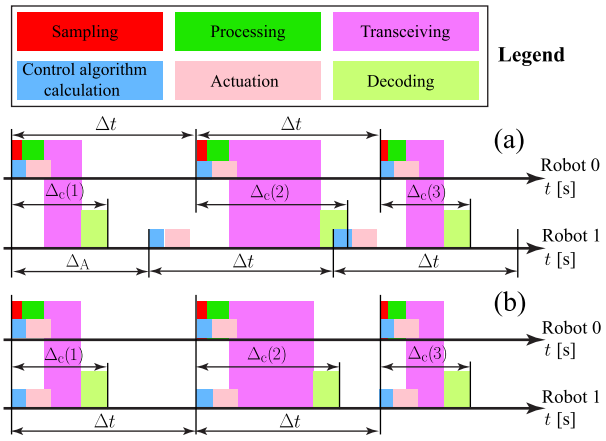

Fig. 17. (a) Control loop misaligned. (b) Control loop perfectly aligned.

different loops. Thus, we will not distinguish it among different loops, i.e., Δ_A is a constant. However, the communication delay $\Delta_c(k)$ is stochastic at each step.

In the first control period shown in Fig. 17(a), the communication delay $\Delta_c(1)$ is less than the alignment error Δ_A. Thus, this data is available before the first control loop starts on robot 1, that is,

$$\Delta_I(1) = \Delta_A \tag{31}$$

where $\Delta_I(k)$ represents the information delay of robot 0 in the controller of robot 1 at k-th control loop. However, in the second control period, the communication delay $\Delta_c(2)$ is greater than the alignment error Δ_A. Thus, this data is not available when the second control loop starts on robot 1. In this case, the robot 1 use the outdated information of robot 0 received previously, resulting in the information delay

$$\Delta_I(2) = \Delta_A + \Delta t. \tag{32}$$

Similarly, the information delay in the third control loop is

$$\Delta_I(3) = \Delta_A. \tag{33}$$

To sum up, we have

$$\Delta_I(k) = \begin{cases} \Delta_A, & \text{if } \Delta_c(k) \le \Delta_A \\ \Delta_A + \Delta t, & \text{if } \Delta_c(k) > \Delta_A. \end{cases} \tag{34}$$

From the perspective of probability, when no packet loss is considered, this information delay satisfies Bernoulli distribution with the probability density function (PDF)

$$f_{\Delta_I(k)}(x) = p\,\delta(x - \Delta_A) + (1-p)\,\delta(x - (\Delta_A + \Delta t)) \tag{35}$$

where $\delta(\cdot)$ is the Dirac delta function, and

$$p = \mathbb{P}(\Delta_c(k) \le \Delta_A). \tag{36}$$

Here, $\mathbb{P}$ is the probability measure.

Fig. 17(b) shows another scheme of three control cycles when the control loops of robots 0 and 1 are perfectly aligned, i.e., $\Delta_A = 0$. In Fig. 18(a), we know that the current state of robot 0 is never available to robot 1 since

$$\mathbb{P}(\Delta_c(k) \le 0) \equiv 0 \tag{37}$$

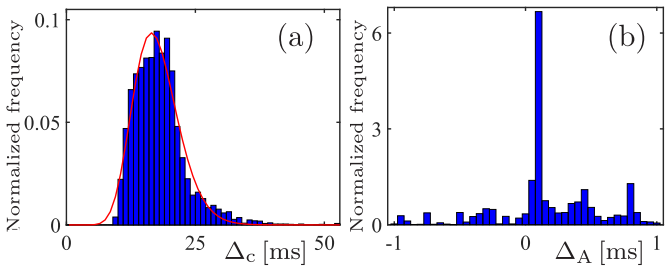

Fig. 18. (a) Histogram of communication delay. (b) Histogram of control loop alignment error.

but the previous state is always almost surely available since

$$\mathbb{P}(\Delta_c(k) \leq \Delta t) = 1 \tag{38}$$

when $\Delta t = 100$ ms is considered in V2V communication. Thus, robot 1 is always almost surely using the information about robot 0 at the previous step, that is, the information delay is deterministic in every loop and equals the sampling time,

$$\Delta_I(k) \equiv \Delta t. \tag{39}$$

In practice, the control loop alignment is not perfect as shown in Fig. 17(b), but can be achieved to certain accuracy by shifting the next control loop based on the current loop alignment error. Fig. 18(b) plots the histogram of this alignment error after this control loop shifting algorithm is implemented. Note that this alignment error reduces to the order of hundreds of microseconds. Indeed, the information delay Δ_I is also a constant in this case as explained in the following.

Fig. 18(a) also shows that the probability of the communication delay over $\Delta_{c,max} \approx 40$ ms or below $\Delta_{c,min} \approx 6$ ms is rather small, due to the fact that the minimum time $\Delta_{c,min}$ is required to go through the whole transceiving process, that is,

$$\mathbb{P}(\Delta_c(k) \leq \Delta_{c,min}) \approx 0 \quad \mathbb{P}(\Delta_c(k) \leq \Delta_{c,max}) \approx 1. \tag{40}$$

Thus, when $\Delta_A \leq \Delta_{c,min}$, the current state of robot 0 is never available; on the other hand, when $\Delta_A \geq -(\Delta t - \Delta_{c,max})$, the previous state is always almost surely available, i.e., the information delay

$$\Delta_I = \Delta t + \Delta_A, \quad -(\Delta t - \Delta_{c,max}) \leq \Delta_A \leq \Delta_{c,min}. \tag{41}$$

Moreover, Δ_A is very small in the experiment as shown in Fig. 18(b), so the control loops are viewed as perfectly aligned and (41) is approximated by (39) for the information delay.

B. Timing Errors

See Table V.

TABLE V
SUMMARY OF TIMING ERRORS

error source	mean value [ms]
clock synchronization error	$\leq 2 \sim 3$
control loop alignment error	≤ 1
period of sensory data processing loop	≤ 4

TABLE VI
CONTROL GAINS FOR DIFFERENT POINTS

point	β [1/s]	α [1/s]	γ [1/s^2]
A	0	1	0.1
B	0.1	1	0.1
C	0.8	1	0.1
D	0.9	1	0.1
E	-0.3	2	0.1
F	-0.4	2	0.1
G	0.3	2	0.1
H	0.4	2	0.1
J	0.9	0.4	0.1
K	0.2	0.3	0.1

C. Matrices Used in Section IV

The matrices used in (14) are

$$\mathbf{A} = \begin{bmatrix} 1 & -\theta_1 & -\gamma\,\theta_4 & -\dfrac{\alpha\,\theta_4}{t_h} & (\alpha+\beta)\,\theta_4 \\ 0 & e^{-c\,\Delta t} & \gamma\,\theta_1 & \dfrac{\alpha\,\theta_1}{t_h} & -(\alpha+\beta)\,\theta_1 \\ \dfrac{\Delta t}{t_h} & -\Delta t & 1 & 0 & 0 \\ 1 & 0 & 0 & 0 & 0 \\ 0 & 1 & 0 & 0 & 0 \end{bmatrix}$$

$$\mathbf{B} = \begin{bmatrix} \theta_2 - \beta\,\theta_4\cos(\omega\,\Delta t) & \theta_3 + \beta\,\theta_4\sin(\omega\,\Delta t) \\ \beta\,\theta_1\cos(\omega\,\Delta t) & -\beta\,\theta_1\sin(\omega\,\Delta t) \\ 0 & 0 \\ 0 & 0 \\ 0 & 0 \end{bmatrix}$$

$$\mathbf{C} = [0 \quad 1 \quad 0 \quad 0 \quad 0] \tag{42}$$

where

$$\theta_1 = \frac{1 - e^{-c\,\Delta t}}{c}, \quad \theta_2 = \frac{\sin(\omega\,\Delta t)}{\omega}$$
$$\theta_3 = \frac{1 - \cos(\omega\,\Delta t)}{\omega}, \quad \theta_4 = \frac{\Delta t - \theta_1}{c}. \tag{43}$$

D. Control Gains in Fig. 7(a)

See Table VI.

E. Human-Driven Vehicles

In another project [72], we have conducted experiments to understand human driving behaviors in real-world scenarios. The GPS positions and velocities of the preceding vehicle and the human-driven vehicle were recorded for analysis. We assumed human drivers follow the dynamics

$$\begin{aligned} \dot{h}_1 &= v_0 - v_1 \\ \dot{v}_1 &= \alpha(V(h_1(t-\tau)) - v_1(t-\tau)) \\ &\quad + \beta(v_0(t-\tau) - v_1(t-\tau)) \end{aligned} \tag{44}$$

TABLE VII
PARAMETERS OF HUMAN DRIVERS

Human parameters	β [1/s]	α [1/s]	τ [s]	$t_{\rm h}$ [s]
Non-scaled	0.3-0.8	0.1-0.4	0.6-1.2	1.0-2.0

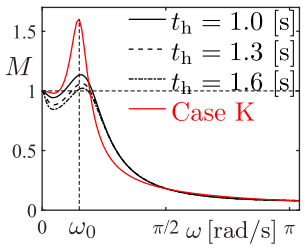

Fig. 19. Comparison between the frequency response of human drivers and the setup in case K [see Fig. 9(a)]. Black curves: frequency responses of human drivers with different time headways. Red curve: frequency response of the setup in case K after rescaling based on Table I.

where τ is the human reaction delay, and the other variables are the same as those used in the main context. By using regression, the parameters given in Table VII can be obtained.

By linearizing (44), we can obtain the transfer function

$$\frac{V_1(s)}{V_0(s)} = \frac{\beta\, s + \frac{\alpha}{t_{\rm h}}}{{\rm e}^{s\tau} s^2 + (\alpha + \beta)\, s + \frac{\alpha}{t_{\rm h}}}. \tag{45}$$

In Fig. 19, we show the frequency response of human drivers using $\beta = 0.55$ [1/s], $\alpha = 0.25$ [1/s], and $\tau = 0.9$ [s] for different time headways $t_{\rm h}$, and compare those to the frequency response of case K explained in the main context. Note that to ensure comparability, the parameters of case K are rescaled based on Table I. It can be seen that the setup in case K and that of human drivers have similar frequency responses except that different human parameters lead to variations in the peak magnitude at ω_0. Still, string unstable behavior is observed in all cases.

ACKNOWLEDGMENT

The authors would like to thank all the members who once worked on Connected Ground Robot Experiment Project.

REFERENCES

[1] D. Schrank, B. Eisele, T. Lomax, and J. Bak, "2015 urban mobility scorecard," Texas A&M Transp. Inst., College Station, TX, USA, Tech. Rep., 2015.
[2] *2016 Fatal Motor Vehicle Crashes: Overview*, USDOT, Nat. Highway Traffic Saf. Admin., Washington, DC, USA, 2017.
[3] H. Winner, *Adaptive Cruise Control*. London, U.K.: Springer, 2012, ch. 24, pp. 613–656.
[4] S. E. Shladover, "Longitudinal control of automotive vehicles in close-formation platoons," *J. Dyn. Syst., Meas., Control*, vol. 113, no. 2, pp. 231–241, 1991.
[5] P. A. Ioannou and C. C. Chien, "Autonomous intelligent cruise control," *IEEE Trans. Veh. Technol.*, vol. 42, no. 4, pp. 657–672, Nov. 1993.
[6] S.-N. Huang and W. Ren, "Design of vehicle following control systems with actuator delays," *Int. J. Syst. Sci.*, vol. 28, no. 2, pp. 145–151, 1997.
[7] R. Rajamani and C. Zhu, "Semi-autonomous adaptive cruise control systems," *IEEE Trans. Veh. Technol.*, vol. 51, no. 5, pp. 1186–1192, Sep. 2002.
[8] J. V. Werf, S. E. Shladover, M. A. Miller, and N. Kourjanskaia, "Effects of adaptive cruise control systems on highway traffic flow capacity," *Transp. Res. Rec., J. Transp. Res. Board*, vol. 1800, no. 1, pp. 78–84, 2002.
[9] L. C. Davis, "Effect of adaptive cruise control systems on mixed traffic flow near an on-ramp," *Phys. A, Stat. Mech. Appl.*, vol. 379, no. 1, pp. 274–290, 2007.
[10] D. de Bruin, J. Kroon, R. van Klaveren, and M. Nelisse, "Design and test of a cooperative adaptive cruise control system," in *Proc. IEEE Intell. Veh. Symp.*, Jun. 2004, pp. 392–396.
[11] E. Uhlemann, "Time for autonomous vehicles to connect [connected vehicles]," *IEEE Veh. Technol. Mag.*, vol. 13, no. 3, pp. 10–13, Sep. 2018.
[12] S. Zhang, J. Chen, F. Lyu, N. Cheng, W. Shi, and X. Shen, "Vehicular communication networks in the automated driving era," *IEEE Commun. Mag.*, vol. 56, no. 9, pp. 26–32, Sep. 2018.
[13] S. K. Datta, J. Haerri, C. Bonnet, and R. F. Da Costa, "Vehicles as connected resources: Opportunities and challenges for the future," *IEEE Veh. Technol. Mag.*, vol. 12, no. 2, pp. 26–35, Jun. 2017.
[14] *IEEE Standard for Wireless Access in Vehicular Environments (WAVE)—Networking Services*, IEEE Standard 1609.3-2010 (Revision of IEEE Standard 1609.3-2007), IEEE Vehicular Technology Society, 2010.
[15] B. Williams, *Intelligent Transport Systems Standards*. Norwood, MA, USA: Artech House, 2008.
[16] A. Festag, "Cooperative intelligent transport systems standards in Europe," *IEEE Commun. Mag.*, vol. 52, no. 12, pp. 166–172, Dec. 2014.
[17] *Intelligent Transport Systems—Dedicated Short Range Communications at 5.8 GHz*, ITU-R Standard M.1453-2, International Telecommunication Union, 2005.
[18] *Intelligent Transport Systems—Dedicated Short Range Communication (DSRC)—DSRC Application Layer*, ISO Standard ISO 15628, International Organization for Standardization, 2013.
[19] *Dedicated Short Range Communications (DSRC) Message Set Dictionary*, SAE Standard J2735, SAE International, 2016.
[20] *Road Transport and Traffic Telematics (RTTT)—Dedicated Short-Range Communication—Profiles for RTTT Applications*, EN Standard CEN-EN 13372, European Committee for Standardization, 2004.
[21] *Dedicated Short-Range Communication (DSRC) Basic Application Interface*, ARIB Standard STD-T110, Association of Radio Industries and Businesses, 2012.
[22] *Cooperation of Roadside to Vehicle—Dedicated Short Range Communications—Part 2: Specification of Medium Access Control Layer and Physical Layer*, SAC Standard GB/T 31024.2-2014, Standardization Administration of China, 2015.
[23] G. Orosz, J. I. Ge, C. R. He, S. S. Avedisov, W. B. Qin, and L. Zhang, "Seeing beyond the line of sight—Controlling connected automated vehicles," *ASME Mech. Eng. Mag.*, vol. 139, no. 12, pp. S8–S12, 2017.
[24] S. Darbha, S. Konduri, and P. R. Pagilla, "Benefits of V2V communication for autonomous and connected vehicles," *IEEE Trans. Intell. Transp. Syst.*, to be published.
[25] J. Siegel, D. Erb, and S. Sarma, "Algorithms and architectures: A case study in when, where and how to connect vehicles," *IEEE Intell. Transp. Syst. Mag.*, vol. 10, no. 1, pp. 74–87, Jan. 2018.
[26] G. J. L. Naus, R. P. A. Vugts, J. Ploeg, M. R. J. G. van de Molengraft, and M. Steinbuch, "String-stable CACC design and experimental validation: A frequency-domain approach," *IEEE Trans. Veh. Technol.*, vol. 59, no. 9, pp. 4268–4279, Nov. 2010.
[27] S. Öncü, N. van de Wouw, and H. Nijmeijer, "Cooperative adaptive cruise control: Tradeoffs between control and network specifications," in *Proc. 14th Int. IEEE Conf. Intell. Transp. Syst. (ITSC)*, Oct. 2011, pp. 2051–2056.
[28] C. Desjardins and B. Chaib-Draa, "Cooperative adaptive cruise control: A reinforcement learning approach," *IEEE Trans. Intell. Transp. Syst.*, vol. 12, no. 4, pp. 1248–1260, Dec. 2011.
[29] G. Guo and W. Yue, "Autonomous platoon control allowing range-limited sensors," *IEEE Trans. Veh. Technol.*, vol. 61, no. 7, pp. 2901–2912, Sep. 2012.
[30] J. Ploeg, D. P. Shukla, N. van de Wouw, and H. Nijmeijer, "Controller synthesis for string stability of vehicle platoons," *IEEE Trans. Intell. Transp. Syst.*, vol. 15, no. 2, pp. 854–865, Apr. 2014.
[31] A. A. Peters, R. H. Middleton, and O. Mason, "Leader tracking in homogeneous vehicle platoons with broadcast delays," *Automatica*, vol. 50, no. 1, pp. 64–74, 2014.
[32] Y. Zheng, S. E. Li, J. Wang, L. Y. Wang, and K. Li, "Stability and scalability of homogeneous vehicular platoon: Study on the influence of information flow topologies," *IEEE Trans. Intell. Transp. Syst.*, vol. 17, no. 1, pp. 14–26, Jan. 2016.
[33] K. C. Dey *et al.*, "A review of communication, driver characteristics, and controls aspects of cooperative adaptive cruise control (CACC)," *IEEE Trans. Intell. Transp. Syst.*, vol. 17, no. 2, pp. 491–509, Feb. 2016.

[34] S. E. Shladover, C. Nowakowski, X.-Y. Lu, and R. Ferlis, "Cooperative adaptive cruise control: Definitions and operating concepts," *Transp. Res. Rec., J. Transp. Res. Board*, vol. 2489, pp. 145–152, Jan. 2015.
[35] B. van Arem, C. J. G. van Driel, and R. Visser, "The impact of cooperative adaptive cruise control on traffic-flow characteristics," *IEEE Trans. Intell. Transp. Syst.*, vol. 7, no. 4, pp. 429–436, Dec. 2006.
[36] V. Milanés, J. Alonso, L. Bouraoui, and J. Ploeg, "Cooperative maneuvering in close environments among cybercars and dual-mode cars," *IEEE Trans. Intell. Transp. Syst.*, vol. 12, no. 1, pp. 15–24, Mar. 2011.
[37] *Cooperative Adaptive Cruise Control: Human Factors Analysis*, USDOT, Federal Highway Administration, Washington, DC, USA, 2013.
[38] J. Ploeg, N. van de Wouw, and H. Nijmeijer, "$\mathcal{L}_p$ string stability of cascaded systems: Application to vehicle platooning," *IEEE Trans. Control Syst. Technol.*, vol. 22, no. 2, pp. 786–793, Mar. 2014.
[39] M. di Bernardo, A. Salvi, and S. Santini, "Distributed consensus strategy for platooning of vehicles in the presence of time-varying heterogeneous communication delays," *IEEE Trans. Intell. Transp. Syst.*, vol. 16, no. 1, pp. 102–112, Feb. 2015.
[40] A. Askari, D. A. Farias, A. A. Kurzhanskiy, and P. Varaiya. (2017). "Effect of adaptive and cooperative adaptive cruise control on throughput of signalized arterials." [Online]. Available: https://arxiv.org/abs/1703.01657
[41] S. E. Shladover *et al.*, "Automated vehicle control developments in the PATH program," *IEEE Trans. Veh. Technol.*, vol. 40, no. 1, pp. 114–130, Feb. 1991.
[42] R. Rajamani and S. E. Shladover, "An experimental comparative study of autonomous and co-operative vehicle-follower control systems," *Transp. Res. C, Emerg. Technol.*, vol. 9, no. 1, pp. 15–31, 2001.
[43] C. Nowakowski, S. E. Shladover, and D. Cody, "Cooperative adaptive cruise control: Testing drivers' choices of following distances," California PATH Program, Inst. Transp. Stud., Berkeley, CA, USA, Res. Rep. UCB-ITS-PRR-2010-39, 2010.
[44] T. H. A. van den Broek, B. D. Netten, M. Hoedemaeker, and J. Ploeg, "The experimental setup of a large field operational test for cooperative driving vehicles at the A270," in *Proc. IEEE 13th Int. Conf. Intell. Transp. Syst.*, Sep. 2010, pp. 198–203.
[45] C. Nowakowski, S. E. Shladover, X.-Y. Lu, D. Thompson, and A. Kailas, "Cooperative adaptive cruise control (CACC) for truck platooning: Operational concept alternatives," Univ. California, Berkeley, Berkeley, CA, USA, Res. Rep., 2015.
[46] E. Chan, "SARTRE automated platooning vehicles," in *Towards Innovative Freight and Logistics*. Hoboken, NJ, USA: Wiley, 2016, ch. 10, pp. 137–150.
[47] J. Ploeg, S. Shladover, H. Nijmeijer, and N. van de Wouw, "Introduction to the special issue on the 2011 grand cooperative driving challenge," *IEEE Trans. Intell. Transp. Syst.*, vol. 13, no. 3, pp. 989–993, Sep. 2012.
[48] C. Englund *et al.*, "The grand cooperative driving challenge 2016: Boosting the introduction of cooperative automated vehicles," *IEEE Wireless Commun.*, vol. 23, no. 4, pp. 146–152, Aug. 2016.
[49] *Taxonomy and Definitions for Terms Related to Driving Automation Systems for on-Road Motor Vehicles*, SAE Standard J3016, SAE International, 2016.
[50] J. I. Ge and G. Orosz, "Dynamics of connected vehicle systems with delayed acceleration feedback," *Transp. Res. C, Emerg. Technol.*, vol. 46, pp. 46–64, Sep. 2014.
[51] L. Zhang and G. Orosz, "Motif-based design for connected vehicle systems in presence of heterogeneous connectivity structures and time delays," *IEEE Trans. Intell. Transp. Syst.*, vol. 17, no. 6, pp. 1638–1651, Jun. 2016.
[52] G. Orosz, "Connected cruise control: Modelling, delay effects, and nonlinear behaviour," *Vehicle Syst. Dyn.*, vol. 54, no. 8, pp. 1147–1176, 2016.
[53] W. B. Qin, M. M. Gomez, and G. Orosz, "Stability and frequency response under stochastic communication delays with applications to connected cruise control design," *IEEE Trans. Intell. Transp. Syst.*, vol. 18, no. 2, pp. 388–403, Feb. 2017.
[54] W. B. Qin and G. Orosz, "Scalable stability analysis on large connected vehicle systems subject to stochastic communication delays," *Transp. Res. C, Emerg. Technol.*, vol. 83, pp. 39–60, Oct. 2017.
[55] S. S. Avedisov and G. Orosz, "Nonlinear network modes in cyclic systems with applications to connected vehicles," *J. Nonlinear Sci.*, vol. 25, no. 4, pp. 1015–1049, Aug. 2015.
[56] L. Zhang and G. Orosz, "Consensus and disturbance attenuation in multi-agent chains with nonlinear control and time delays," *Int. J. Robust Nonlinear Control*, vol. 27, no. 5, pp. 781–803, 2017.
[57] J. I. Ge and G. Orosz, "Optimal control of connected vehicle systems with communication delay and driver reaction time," *IEEE Trans. Intell. Transp. Syst.*, vol. 18, no. 8, pp. 2056–2070, Aug. 2017.
[58] C. R. He, W. B. Qin, N. Ozay, and G. Orosz, "Optimal gear shift schedule design for automated vehicles: Hybrid system based analytical approach," *IEEE Trans. Control Syst. Technol.*, vol. 26, no. 6, pp. 2078–2090, Nov. 2018.
[59] T. G. Molnár, W. B. Qin, T. Insperger, and G. Orosz, "Application of predictor feedback to compensate time delays in connected cruise control," *IEEE Trans. Intell. Transp. Syst.*, vol. 19, no. 2, pp. 545–559, Feb. 2018.
[60] G. Stépán, "Vibrations of machines subjected to digital force control," *Int. J. Solids Struct.*, vol. 38, nos. 10–13, pp. 2149–2159, 2001.
[61] M. Di Vaio, G. Fiengo, A. Petrillo, A. Salvi, S. Santini, and M. Tufo, "Cooperative shock waves mitigation in mixed traffic flow environment," *IEEE Trans. Intell. Transp. Syst.*, to be published.
[62] M. Won, T. Park, and S. H. Son, "Toward mitigating phantom jam using vehicle-to-vehicle communication," *IEEE Trans. Intell. Transp. Syst.*, vol. 18, no. 5, pp. 1313–1324, May 2017.
[63] Y. Zheng, S. Li, K. Li, and L.-Y. Wang, "Stability margin improvement of vehicular platoon considering undirected topology and asymmetric control," *IEEE Trans. Control Syst. Technol.*, vol. 24, no. 4, pp. 1253–1265, Jul. 2016.
[64] S. Stüdli, M. M. Seron, and R. H. Middleton, "From vehicular platoons to general networked systems: String stability and related concepts," *Annu. Rev. Control*, vol. 44, pp. 157–172, 2017.
[65] B. Besselink and K. H. Johansson, "String stability and a delay-based spacing policy for vehicle platoons subject to disturbances," *IEEE Trans. Autom. Control*, vol. 62, no. 9, pp. 4376–4391, Sep. 2017.
[66] A. Talebpour and H. S. Mahmassani, "Influence of connected and autonomous vehicles on traffic flow stability and throughput," *Transp. Res. C, Emerg. Technol.*, vol. 71, pp. 143–163, Oct. 2016.
[67] *IEEE Standard for a Precision Clock Synchronization Protocol for Networked Measurement and Control Systems*, IEEE Standard 1588-2008 (Revision of IEEE Std 1588-2002), IEEE Instrumentation and Measurement Society, 2008.
[68] D. Mills, *Simple Network Time Protocol (SNTP) Version 4 for IPv4, IPv6 and OSI*, document RFC 4330, Network Working Group, 2006.
[69] M. Ussoli and G. Prytz, "SNTP time synchronization accuracy measurements," in *Proc. IEEE 18th Conf. Emerg. Technol. Factory Automat. (ETFA)*, Sep. 2013, pp. 1–4.
[70] J. B. Kenney, "Dedicated short-range communications (DSRC) standards in the United States," *Proc. IEEE*, vol. 99, no. 7, pp. 1162–1182, Jul. 2011.
[71] S. Gao, A. Lim, and D. Bevly, "An empirical study of DSRC V2V performance in truck platooning scenarios," *Digit. Commun. Netw.*, vol. 2, no. 4, pp. 233–244, 2016.
[72] J. I. Ge and G. Orosz, "Connected cruise control among human-driven vehicles: Experiment-based parameter estimation and optimal control design," *Transp. Res. C, Emerg. Technol.*, vol. 95, pp. 445–459, Oct. 2018.

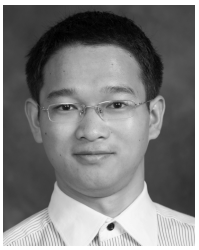

Wubing B. Qin received the B.Eng. degree from the School of Mechanical Science and Engineering, Huazhong University of Science and Technology, Wuhan, China in 2011, and the M.Sc. and Ph.D. degrees in mechanical engineering from the University of Michigan, Ann Arbor, MI, USA, in 2016 and 2018, respectively.

In 2018, he joined Aptiv, Troy, MI, USA, where he is currently an ADAS Algorithm Developer. His current research interests include dynamics and control of connected vehicles, digital systems, ground robotics, and nonlinear and stochastic systems with time delays.

Gábor Orosz received the M.Sc. degree in engineering physics from the Budapest University of Technology, Budapest, Hungary, in 2002, and the Ph.D. degree in engineering mathematics from the University of Bristol, Bristol, U.K., in 2006.

He held postdoctoral positions at the University of Exeter, Exeter, U.K., and the University of California at Santa Barbara, Santa Barbara, CA, USA. In 2010, he joined the University of Michigan, Ann Arbor, MI, USA, where he is currently an Associate Professor in mechanical engineering. His current research interests include nonlinear dynamics and control, time delay systems, and networks and complex systems with applications on connected and automated vehicles and biological networks.